RESEARCH ARTICLE

Paramagnetic nanoparticles as potential MRI contrast agents: characterization, NMR relaxation, simulations and theory

**Quoc Lam Vuong · Sabine Van Doorslaer · Jean-Luc Bridot ·
Corradina Argante · Gabriela Alejandro · Raphaël Hermann ·
Sabrina Disch · Carlos Mattea · Siegfried Stapf · Yves Gossuin**

Abstract

Object Paramagnetic nanoparticles, mainly rare earth oxides and hydroxides, have been produced these last few years for use as MRI contrast agents. They could become an interesting alternative to iron oxide particles. However, their relaxation properties are not well understood.

Materials and methods Magnetometry, ^{1}H and ^{2}H NMR relaxation results at different magnetic fields and electron paramagnetic resonance are used to investigate the relaxation induced by paramagnetic particles. When combined with computer simulations of transverse relaxation, they allow an accurate description of the relaxation induced by paramagnetic particles.

Results For gadolinium hydroxide particles, both T_1 and T_2 relaxation are due to a chemical exchange of protons between the particle surface and bulk water, called inner sphere relaxation. The inner sphere is also responsible for the T_1 relaxation of dysprosium, holmium, terbium and erbium containing particles. However, for these latter compounds, T_2 relaxation is caused by water diffusion in the field inhomogeneities created by the magnetic particle, the outer-sphere relaxation mechanism. The different relaxation behaviors are caused by different electron relaxation times (estimated by electron paramagnetic resonance).

Conclusion These findings may allow tailoring paramagnetic particles: ultrasmall gadolinium oxide and hydroxide particles for T_1 contrast agents, with shapes ensuring the highest surface-to-volume ratio. All the other compounds present interesting T_2 relaxation performance at high fields. These results are in agreement with computer simulations and theoretical predictions of the outer-sphere and static dephasing regime theories. The T_2 efficiency would be optimum for spherical particles of 40–50 nm radius.

Q. L. Vuong · C. Argante · Y. Gossuin (✉)
Biological Physics Department, University of Mons—UMONS,
20 Place du Parc, 7000 Mons, Belgium
e-mail: yves.gossuin@umons.ac.be; yves.gossuin@umons.be

S. Van Doorslaer · G. Alejandro
Department of Physics, University of Antwerp, Antwerp,
Belgium

J.-L. Bridot
Department of Chemistry, Université Laval, Quebec City,
QC G1V 0A6, Canada

J.-L. Bridot
Centre de Recherche sur les Matériaux Avancés (CERMA),
Université Laval, Quebec City, QC, Canada

G. Alejandro
Centro Atómico Bariloche (CNEA) and CONICET,
8400 San Carlos de Bariloche, Argentina

R. Hermann · S. Disch
Institut für Festkörperforschung, JCNS und JARA-FIT,
Forschungszentrum, Jülich GmbH, Jülich, Germany

R. Hermann
Faculté des Sciences, Université de Liège, Liège, Belgium

C. Mattea · S. Stapf
Fakultät für Mathematik und Naturwissenschaften,
FG Technische Physik II/Polymerphysik, Technische Universität
Ilmenau, Ilmenau, Germany

Introduction

For specific applications, such as molecular and cellular imaging, magnetic resonance imaging (MRI) requires the use of contrast agents despite its excellent intrinsic contrast [1]. The more efficient the contrast agent is, the more sensitive the detection (of tagged cells or targeted tumors, for example) will be. Besides the efforts in improvement of classical contrast agents, such as paramagnetic ion complexes [2] and iron oxide superparamagnetic particles [3], there is a growing interest in the development of paramagnetic particles [4–7] and their characterization [8, 9]. Paramagnetic rare-earth-containing particles (oxides, hydroxides, fluorides …) may be produced by a variety of processes [10–14]. They are used for their catalytic activity [15] or their photoluminescent properties [16–20], but their paramagnetic behavior opens many perspectives in MRI and multimodal optical/MR imaging [21–25]. While iron-oxide nanoparticles at body temperature (310 K) are ferrimagnetic crystals ($T_{\text{Néel}} > 310$ K) in the superparamagnetic regime ($T_{\text{B}} < 310$ K) [26], paramagnetic particles are constituted of rare-earth oxide or hydroxide with a Curie temperature (T_{C}) far below room temperature. Hence, at room temperature, these particles are purely paramagnetic [27]. Their magnetization is following a classical Langevin function, but the magnetic saturation is not expected at the magnetic fields used for MRI. Their magnetization is simply increasing linearly with the field, as predicted by the Langevin function at low fields. At first sight, these paramagnetic particles do not appear to be excellent candidates for building efficient contrast agents; their magnetic moment is indeed not maximal while superparamagnetic particles present a magnetic moment aligned with the field at ca 0.2 T. Similar as for iron oxide, the use of particles is especially interesting for molecular targeting and cellular imaging applications [28]: by bringing one particle to the desired region of the body or in the cell of interest, one transports thousands of magnetic ions at once, ensuring a large relaxation effect [29]. Moreover, even if the paramagnetic moment is small at the usual fields, it could become equal and even larger to superparamagnetic moments at larger magnetic fields. Indeed, iron oxide particles are ferrimagnetic, which means that they contain two magnetic lattices with opposite magnetic orientations (partially compensating) whose resultant magnetic moment constitutes the magnetic moment of the particle [30]. For paramagnetic particles, when approaching magnetic saturation, all the paramagnetic ions constituting the particles will finally align in the field, resulting in a very large magnetic moment for the particle. Of course, as previously mentioned, the particles are far from saturation, but a rough calculation shows that their molar magnetization is already comparable to the one of iron oxide particles at about 10 T.

Especially for dysprosium- or holmium-containing particles, the maximum magnetization will be the largest achievable since these ions have the largest individual magnetic moment (~ 10 Bohr magnetons).

In recent years, different groups [31–35] have produced and characterized paramagnetic rare-earth-containing particles, reporting interesting properties for MRI. Gadolinium oxide and hydroxide particles were shown to present rather efficient T_1 relaxation, with relaxivities ranging from 4 to 40 s^{-1} mM^{-1} at 1.5 T. On the contrary, dysprosium oxide particles have almost negligible longitudinal relaxivity at all fields, but they could represent an alternative T_2 contrast agent, especially for high magnetic fields, since their transverse relaxivity increases with the field as first shown at high fields by Norek et al. [7] and later confirmed at low and intermediate fields and also for gadolinium hydroxide particles [9]. However, T_1 and T_2 relaxation mechanisms of water in the presence of these particles has never been studied in detail except by Peters et al. for T_2 and particles in xanthan gum [7] and by our group only for gadolinium hydroxide and dysprosium-oxide particles [9], with incomplete conclusions. It should be mentioned that one major drawback of the paramagnetic particles is their possible toxicity. Indeed, without appropriate coating, they could release free rare-earth ions in vivo with disastrous consequences (comparable to nephrogenic systemic fibrosis for patients with kidney failure) [36].

In this article, we present transmission electron microscopy (TEM), magnetometric, electron paramagnetic resonance (EPR) and NMR ^{1}H and ^{2}H relaxation results for $Ho_4O(OH)_9NO_3$, $Er_4O(OH)_9NO_3$ and Tb_4O_7 particles dispersions. The transverse relaxation induced by paramagnetic particles—caused by the diffusion of protons around the particle—was also simulated by a well established Monte Carlo algorithm for a large range of particle sizes and at different magnetic fields. New EPR and ^{2}H NMR results are also presented for $Gd(OH)_3$ and Dy_2O_3 particles. Relaxation theoretical models are finally confronted to the experimental and simulation data allowing a better understanding of the T_1 and T_2 relaxation, which is of importance for the development of optimal paramagnetic particles.

Materials and methods

Dysprosium oxide, gadolinium hydroxide, holmium oxide and erbium oxide particles dispersions (dispersive agent: 1 % Disperbyk, commercial high molecular weight block copolymer) were purchased from Sigma-Aldrich (ref 639664, 641871, 641863, 641839 respectively). The terbium oxide particles dispersion was prepared with terbium oxide nanopowder (Sigma-Aldrich ref 634255), distilled water and the Disperbyk dispersant agent. All the solutions

for the NMR measurements were prepared using distilled water. For the T_1-NMRD profiles, highly concentrated solutions were used (up to 200 mM for Dy_2O_3 particles). pH of the solutions was about 7. The very low concentration of free rare-earth ions in the solutions was checked by dialysis and subsequent colorimetric analysis: the initial solutions were dialyzed and the low concentration of rare-earth ions in dialysis water was checked by the Arsenazo III colorimetric test. However, one cannot exclude the presence of a small quantity of free ions in our solutions. For example, the solubility of gadolinium hydroxide is about 1.88×10^{-4} g/l, which corresponds to a maximum Gd^{3+} concentration of 1 μM. Such a concentration would not have been detected by the colorimetric test. For the other compounds, this concentration could be slightly higher, depending on the solubility. Fortunately, the influence of these free ions on the relaxation rates of the studied dispersions is negligible. A mixture of distilled water and methanol was used to discriminate between exchange and diffusion relaxation mechanism. For ^{2}H-NMRD, the samples were prepared with 99.9 % deuterium oxide to obtain a large deuterium signal (Sigma-Aldrich ref 613444).

Transmission Electron Microscopy observations and electronic diffraction were realized with a CM 20 Philips microscope and a FEI Tecnai 12. Photon Correlation Spectroscopy (PCS) was used to determine the hydrodynamic size of the particles (Zêtasizer Nanoseries ZEN 3600, Malvern, UK). High field magnetometry curves (up to 8.5 T) were recorded with the Vibrating Sample Magnetometer (VSM) option of a Quantum Design Physical Property Measurement System at 37 °C. The Tb_4O_7 magnetometric data was obtained with a mini high field VSM measurement system of Cryogenics, UK. X-ray diffraction was performed on a Siemens D5000 diffractometer with a Cu Kα source.

X-band (9.44 GHz) continuous-wave EPR spectra were recorded on a Bruker ESP300E instrument, equipped with a liquid Helium cryostat (Oxford Inc.) that allows cooling down to 2.5 K. A modulation frequency of 100 kHz was used. Microwave power, modulation amplitude and measurement temperature were as indicated in the figure captions. The particle dispersions were inserted in a quartz tube with i.d. 0.6 mm and o.d. 0.84 mm that was in turn put in a standard X-band quartz tube (OD 4 mm). The simulations were performed using the EasySpin program [37].

Relaxation time measurements were performed at low fields on BRUKER (Germany) PC110, mq 20, PC140, mq 60 instruments and a Spintrack relaxometer operating at magnetic fields (B_0) of 0.24, 0.47, 0.94, 1.41 and 0.67 T respectively. BRUKER AVANCE-200 (4.7 T), BRUKER AMX 300 (7 T) and AMX 500 (11.7 T) spectrometers were used for the high-field measurements. T_1 relaxation profiles were recorded at 5 °C (^{1}H) and 37 °C (^{1}H and ^{2}H) from 0.00023 to 0.23 T on a Spinmaster fast field cycling relaxometer (STELAR, Mede, Italy). Except for the other mention in the figure legend, all the relaxation measurements were performed at 37 °C. The echo-time used in the CPMG sequence for the determination of T_2 was fixed to 1 ms. The results are represented as longitudinal and transverse relaxivities, which are defined by the increase in the longitudinal and transverse relaxation rates due to an increase of 1 mM in the paramagnetic ion concentration. T_2^* was not measured for our samples. Indeed, different tests on the high-resolution spectrometers showed that even for reference solutions (simply containing gadolinium ions, for example), the value of T_2^* evaluated with the line-width of the resonance peak was often significantly lower than the T_2 value, while for such systems T_2 and T_2^* should be identical. During our tests, the influence of the shims seemed to be critical for paramagnetic particles when estimating T_2^* maybe because of the magnetic field homogeneities created by the particles or the presence of dispersant in our samples. A "real" T_2^*, comparable to the value predicted by the different microscopic relaxation theories, could be very difficult to obtain. The erbium, holmium and terbium content of the samples were determined using Inductively Coupled Plasma (ICP) spectroscopy (Thermo, USA), after microwave mineralization of the suspensions with a mixture of nitric acid and hydrogen peroxide.

The simulation programs were written in C++. The main steps of the algorithm were already described elsewhere [38] and validated in [39]: briefly, a distribution of paramagnetic particles is generated; random walks of several protons model their diffusion in the sample. The space jump is related to time intervals by the well-known relation

$$\delta = \sqrt{6D\Delta t} \tag{1}$$

where D is the diffusion coefficient. Paramagnetic particles are assumed to be impenetrable. After a 90° pulse, the spin dephasing due to the dipolar magnetic field is calculated at each time step for each proton by the following equation:

$$B_{tot,z}(\vec{r}) = \sum_{i=\text{paramagnetic particles}} B_{loc,z}(r_i, \theta_i);$$

$$B_{loc,z}(r, \theta) = R^3 B_{eq} \frac{3\cos^2\theta - 1}{r^3} \tag{2}$$

where R is the radius of the particle, r is the distance between the proton and the paramagnetic particle, θ is the angle between the vector joining the proton to the paramagnetic particle and the direction of the field (z-axis by convention). A Carr–Purcell–Meiboom–Gill sequence is simulated by computing the macroscopic nuclear magnetic moment and considering the 180° echo pulse. The simulated echoes are recorded and then fitted, giving the relaxation rate R_2 of the

system. The following simulation parameters were used: the periodic simulation space was composed of 25×27 paramagnetic particles for the uniform distribution case. In the linear one, 50×27 aggregates were generated. The space step was chosen equal to the paramagnetic radius. A volume fraction of 2×10^{-5} was used. It corresponds to approximately 0.85 mM depending on the density of the different particles. For each simulation, 8,000–20,000 protons were generated. Echo time was fixed at 1 ms. 2 or 3 different simulations were computed for each set of physical parameters. The error bars shown on the curves correspond to twice the standard deviation.

Results

The XRD patterns (Fig. 1) of the holmium- and erbium-containing particles is similar to the spectrum of the yttrium-containing system $Y_4O(OH)_9NO_3$ [40, 41], which could be obtained during the synthesis of yttrium oxide. Indeed, the positions of the peaks are perfectly matching those of the $Y_4O(OH)_9NO_3$ pattern. It was already shown that a similar ytterbium-containing mineral ($Yb_4O(OH)_9 NO_3$) also existed [42]. The erbium- and holmium-containing particles used in this work are thus composed of $Er_4O(OH)_9NO_3$ and $Ho_4O(OH)_9NO_3$. The terbium-containing particles display diffraction peaks characteristic of pure face-centered cubic Tb_4O_7 [43]. The hydrodynamic size of the particles was 250 nm for the holmium-containing particles, 1,500 nm for the erbium-containing particles and 180 nm for the terbium-containing particles. TEM pictures (Fig. 2) confirm these values and clearly show the rod-like morphology of the particles. The use of the hydrodynamic size in the rest of the paper is questionable, because of the shape of the particles. Indeed for non spherical particles, the hydrodynamic size underestimates the largest dimension of the particle. However, it will be employed for the qualitative comparison of the different samples.

The magnetic susceptibilities obtained by a linear regression of the magnetization data at varying magnetic fields (Fig. 3) are provided in Table 1. They are compatible with the known values of these paramagnetic rare-earth ions [44].

Water–methanol dispersions of $Ho_4O(OH)_9NO_3$, $Er_4O(OH)_9NO_3$ and terbium-oxide particles were prepared in order to determine the relaxation mechanism, following a previously described protocol [45]. This experimental procedure was developed to distinguish exchange and diffusion relaxation mechanisms. The test discriminates according to the character of the transverse or longitudinal relaxation in water–methanol solutions: a mono-exponential decay corresponds to diffusion, while a bi-exponential decay indicates the contribution of a proton exchange. In
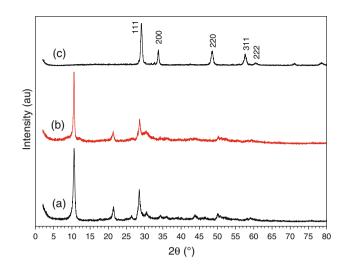

Fig. 1 XRD spectra obtained for the (a) holmium-, (b) erbium- and (c) terbium-containing particles

this latter case, OH protons correspond to the fast component of the bi-exponential curve—because of their proximity with the magnetic ion—while CH protons constitute the slow fraction. The return to equilibrium of the longitudinal magnetization is clearly bi-exponential for the three compounds, which proves the occurrence of a proton exchange in the longitudinal relaxation process. The evolution of the transverse magnetization in a CPMG spin echo sequence for the water–methanol solutions of the holmium-, erbium- and terbium-containing particles is purely mono-exponential, which shows that transverse relaxation is caused by the diffusion of protons nearby the paramagnetic particles.

The longitudinal NMRD relaxation profiles of terbium oxide, and erbium- and holmium-containing particles dispersions are shown in Fig. 4. A Lorentzian function (3a) was fitted to the ^1H data and a sum of Lorentzian functions (3b) for the ^2H data [46]:

$$r_1 = k_0 + k_1 \frac{\tau}{1 + (\omega\tau)^2} \tag{3a}$$

$$r_1 = k_0 + k_1 \left[0.2 \frac{\tau}{1 + (\omega\tau)^2} + 0.8 \frac{\tau}{1 + (2\omega\tau)^2} \right] \tag{3b}$$

In Eq. 3a, ω is either the protonic (ω_0) or the electron Larmor angular frequency (ω_S) depending on the origin of the relaxation process, with $\omega_S = 658 \, \omega_0$. In Eq. 3b, it represents the deuterium Larmor angular frequency. τ is the correlation time associated with the dispersion and k_0, k_1 are, respectively, the offset and the amplitude of the dispersion. The obtained values for τ, considering that $\omega = \omega_0$ for ^1H NMRD are given in Table 2, as well as the values previously reported for gadolinium hydroxide and dysprosium oxide particles.
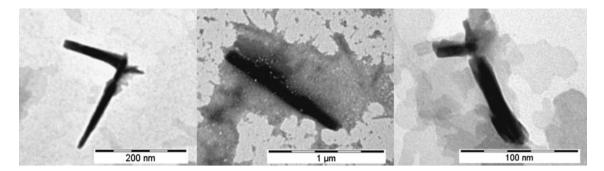
Fig. 2 Transmisson electron microscopy of $Ho_4O(OH)_9NO_3$ (*left*), $Er_4O(OH)_9NO_3$ (*middle*) and Tb_4O_7 (*right*) nanoparticles
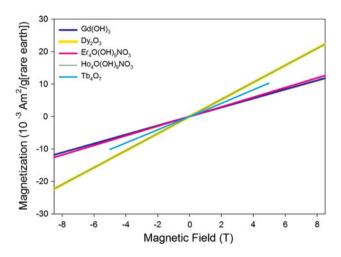

Fig. 3 High-field magnetometry of the $Ho_4O(OH)_9NO_3$, $Er_4O(OH)_9$ NO_3 and Tb_4O_7 nanoparticles. Previous results obtained for Dy_2O_3 and $Gd(OH)_3$ are also shown for comparison

The evolution of transverse relaxation rates with the magnetic field is of special interest for paramagnetic particles, whose magnetic moment increases linearly with the magnetic field. Figure 5 presents the evolution of the transverse relaxation rate of the different paramagnetic particles with the magnetic field, for a volume fraction of particles of 2×10^{-5}. In fact, to allow facile comparison between the different compounds and also with the simulation results, the magnetic field is expressed in terms of the particle's equatorial field, which is proportional to the magnetic field for such paramagnetic compounds. For each type of particle, the proportionality constant between the

equatorial field and the external field is different. It was calculated from the susceptibility values provided in Table 1. Figure 5 also presents the predictions of the different relaxation theories for different particle sizes, i.e. the outer-sphere model (OSM, Eq. 4) and the static dephasing regime (SDR, Eq. 5).

$$R_2 = \frac{16}{45}\tau_D f(\Delta\omega)^2 \quad \text{with } \Delta\omega = \frac{\gamma\mu_0 M}{3}$$

$$R_2 = \frac{16}{405}\tau_D f\gamma^2\mu_0^2 M^2 = \frac{16}{405}\tau_D f\gamma^2\chi^2 B_0^2 \tag{4}$$

$$R_2^* = \frac{2\pi}{3\sqrt{3}}f\Delta\omega \approx R_2$$

$$R_2 = \frac{2\pi}{9\sqrt{3}}f\gamma\mu_0 M = \frac{2\pi}{9\sqrt{3}}f\gamma\chi B_0 \tag{5}$$

where $\tau_D = R^2/D$. $D = 3 \times 10^{-9}$ m²/s is the water diffusion coefficient at 310 K. Eq. 5 is only exact for R_2^*. Nevertheless, it also provides a good estimate [39] of the maximum R_2 when $5 < \Delta\omega\tau_D < 20$.

The simulated T_2 values for particles of different sizes are presented in the same graph. Some of the corresponding relaxivities (experience and simulation) are provided for two different magnetic fields in Table 3. The sizes were chosen to obtain approximately the same volume as our samples.

The effect of the particle shape was also investigated thanks to simulations. Figure 6 presents the $1/T_2$ values obtained for five different systems: a spherical particle with a radius of 50 nm and linear aggregates of 5, 10, 20 and 50 particles with radius of respectively 29.4, 23.2, 18.4 and

Table 1 Magnetic susceptibilities of the samples

Sample	Ion μ_{eff} (μ_β)	Particle size (nm)		Mass susceptibility χ_M (Am²/[Tg(ion)])	Volume susceptibility χ
Gd(OH)$_3$—Gossuin et al. [9]	7.94	150	37 °C	1.42×10^{-3}	0.0113
Dy$_2$O$_3$—Gossuin et al. [9]	10.6	160		2.63×10^{-3}	0.0224
Ho$_4$O(OH)$_9$NO$_3$	10.6	250		2.62×10^{-3}	0.0183
Er$_4$O(OH)$_9$NO$_3$	9.6	1,500		1.48×10^{-3}	0.0104
Tb$_4$O$_7$	9.7	180	25 °C	1.80×10^{-3}	0.0141

Fig. 4 **a** Evolution of the longitudinal relaxivity of $Ho_4O(OH)_9NO_3$, $Er_4O(OH)_9NO_3$ and Tb_4O_7 nanoparticles suspensions with the external magnetic field. Previous results [9] obtained for Dy_2O_3 and $Gd(OH)_3$ are also shown for comparison. The *lines* are Lorentzian fittings of the data. **b** ^{2}H-longitudinal NMRD profiles of the same samples. The *lines* are Lorentzian fittings of the data
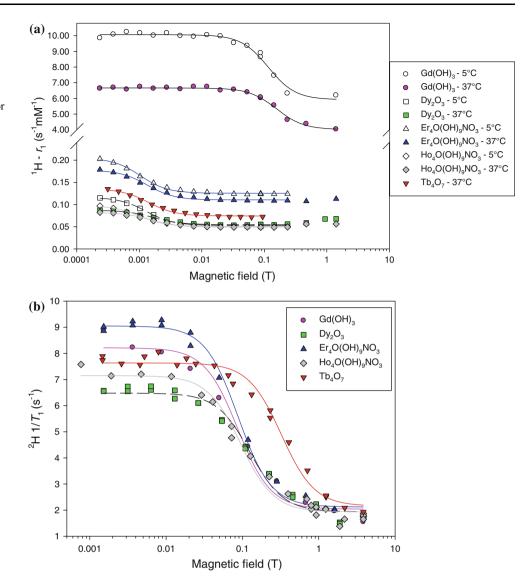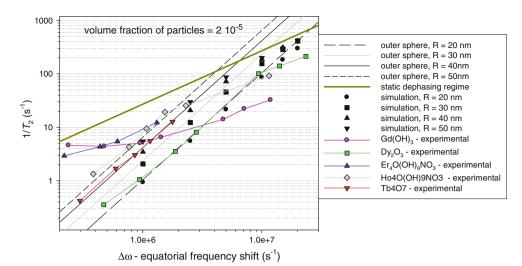

Table 2 Correlation times obtained from the ^{1}H and ^{2}H-NMRD profiles

	^{1}H-NMRD, correlation time τ (µs)		^{2}H-NMRD, correlation time τ (µs)
	37 °C	5 °C	37 °C
$Gd(OH)_3$	0.0239 [9]	0.0323 [9]	1.06
Dy_2O_3	2.25 [9]	2.88 [9]	0.72
$Ho_4O(OH)_9NO_3$	2.44	3.65	0.95
$Er_4O(OH)_9NO_3$	2.79	3.60	1.04
Tb_4O_7	2.65	–	0.28

13.6 nm. These radius values were chosen in order to obtain the same total particle volume in the clusters as for the initial 50 nm sphere. Linear clusters were supposed to be aligned with the static field. Satoh et al. [47] showed that at equilibrium, magnetic spheres tend to form linear chains

whose axes are parallel to the magnetic field. Thus, if we picture the paramagnetic rods as dense liner chains of small particles, they can be supposed to be aligned with the field. However, results for random orientations of the chains are also presented for comparison. Figure 6 shows clearly that a spherical shape induces higher relaxation rate and is thus more efficient from the relaxation point of view, which was also observed in a previous study [39].

The gadolinium hydroxide suspensions show clear EPR spectra from room temperature down to low temperature (10 K) (Fig. 7). At 10 K, the spectrum consists of a broad feature at $g \approx 2$ and feature at $g \approx 6.4$ (Fig. 7a). The spectrum does not show saturation up to 200 mW microwave power (spectrometer upper limit of the microwave power). The spectrum is similar to the spectra that have been observed in zeolitic nanoparticles with relatively high Gd^{3+} doping [48]. This type of EPR spectra of Gd^{3+} in glassy systems have been shown to originate from a broad

Fig. 5 Evolution of the transverse relaxation rate of $Ho_4O(OH)_9NO_3$, $Er_4O(OH)_9NO_3$ and Tb_4O_7 nanoparticles suspensions with the equatorial frequency shift of the particle $\Delta\omega$. Since $\Delta\omega$ linearly increases with the magnetic field, the *horizontal axis* can also be considered as a magnetic field axis. However, a single magnetic field value corresponds to a different $\Delta\omega$ value for each compound since the proportionality constant between $\Delta\omega$ and the field is different for each compound (see supplementary material). Previous results [9] obtained for Dy_2O_3 and $Gd(OH)_3$ are shown for comparison. The relaxation rates obtained by computer simulations for different particle sizes are also presented. Theoretical predictions of the outer-sphere theory and static dephasing regime are represented by the lines. All the results were normalized to a particles volumetric fraction of 2×10^{-5}

Table 3 Transverse relaxivity of the different samples at two magnetic fields

	r_2—1.5 T ($s^{-1}mM^{-1}$)	r_2—7 T ($s^{-1}mM^{-1}$)
$Gd(OH)_3$	7.99	27.1
Dy_2O_3	9.66	168
$Ho_4O(OH)_9NO_3$	27.2	104
$Er_4O(OH)_9NO_3$	4.28	–
Tb_4O_7	16.3	–
Dy_2O_3 Spheres simulation, R = 20 nm	6.6 (1.19 T)	219
Dy_2O_3 Spheres simulation, R = 40 nm	24.9 (1.19 T)	373 (7.14 T)

unimodal distribution of second-order crystal-field parameters and of asymmetry parameters [49]. Furthermore, the $g \approx 2$ signal also has contributions of dipolarly interacting Gd^{3+} sites due to the short distance between two neighboring Gd ions (3.6 Å) [50]. The room-temperature X-band EPR spectrum of the gadolinium hydroxide nanoparticles in suspension are dominated by a Lorentzian resonance at $g \approx 1.963$ overlaying a broader line around $g \approx 2$ (Fig. 7b). The latter most probably results from precipitated nanoparticles (compare also to the low-temperature EPR spectrum in Fig. 7a), while the former dominant contribution is due to rotational averaging of the various anisotropic interactions (electron Zeeman, zero-field and hyperfine interactions) [48]. This allows estimating the electronic transverse relaxation rate, $1/\tau_{2e}$ [48, 51–53].

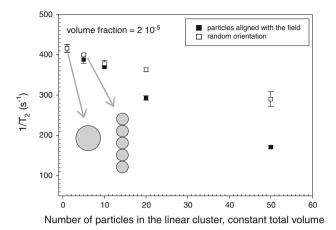$$\frac{1}{\tau_{2e}} = \frac{g\mu_B\pi\sqrt{3}}{h}\Delta H_{pp} \tag{6}$$

with μ_B the Bohr magneton and ΔH_{pp} the peak-to-peak EPR line width (=38 ± 5 mT). τ_{2e} is then estimated to be 176 ± 20 ps (at ~0.34 T).

The other nanoparticle suspensions were found to exhibit no room-temperature CW-EPR spectrum.

At 2.25 K, a clear EPR feature is found for the frozen suspension of $Er_4O(OH)_9NO_3$ particles, a signal that was found to disappear fast at higher temperatures (no signal could be observed at 70 K), indicative of short electronic relaxation times (Fig. 1 supplementary material). The spectrum consists of a broad line around 100 mT, a feature that has also been found for nanostructured $SnO_2:SiO_2$ glass ceramics with Er doping [54] and for erbium-doped β-PbF_2 nanocrystals in transparent glass–ceramics [55]. The observation of the broad powder-like resonance with main resonance at $g \approx 6.7$ is indicative of the $^4I_{15/2}$ ground state [55, 56], while the considerable line-broadening can be ascribed to dipolar interactions between the Er^{3+} sites.

The powder of terbium-oxide nanoparticles exhibits a broad EPR spectrum at $g \approx 2$ with a lorentzian shape and linewidth of 46 mT (Fig. 2 supplemental material). This signal arises from the Tb^{4+} sites [56] and the line broadening and weak signal is again due to the close proximity of the different Tb^{4+} sites.

The 2.3 K CW-EPR spectrum of the dysprosium oxide particles shows very weak features in a broad magnetic field range [0–750 mT] (not shown), that are hardly

Fig. 6 Effect of the shape of the particles on the transverse relaxation. The transverse relaxation rate is presented for different systems with the same total volume but with different geometrical configurations; a unique sphere or linear arrangements of spheres in order to mimic rod-like particles. The data are presented for random and aligned orientations of the "rods". The equatorial field of the particles is 7.5×10^{-2} T and the volumetric fraction of the particles is 2×10^{-5}
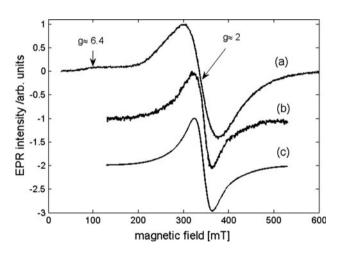

Fig. 7 CW-EPR spectrum of a suspension of gadolinium hydroxide nanoparticles (a) at 10 K and (b) at room temperature. The EPR spectra were recorded with a microwave power of (a) 100 mW and (b) 2 mW. A modulation amplitude of 0.8 mT was used. (c) shows the simulation of (b) assuming a Lorentzian line with linewidth of 38 mT and a minority broad back simulated here as a single Gaussian line with linewidth 115 mT

distinguishable from the background. For Dy^{3+} ($^6H_{15/2}$) doped systems, a variety of g values have been reported ranging from no EPR signal in the ground state up to resonance lines at (apparent) g values of 2.6–14 depending on the local symmetry [56].

No EPR signals of the $Ho_4O(OH)_9NO_3$ particle suspensions could be observed, even at the lowest temperatures.

Discussion

Magnetic properties

Contrarily to iron oxide particles whose magnetic properties dramatically depends on the synthesis process, the purity and the size of the obtained crystals, the magnetism of rare-earth based particles is only depending on the type of paramagnetic ion. The highest magnetization is obtained for dysprosium- and holmium-containing particles. It should be stressed that the nature of the particles and their crystallinity is not a crucial parameter since the Curie temperature of these compounds is very low: rare-earth phosphates or fluorides could be used instead of oxides or hydroxides with approximately the same magnetic properties. This is, of course, not true with iron oxide particles which could be anti-ferromagnetic or ferrimagnetic for different type of oxides and hydroxides [9].
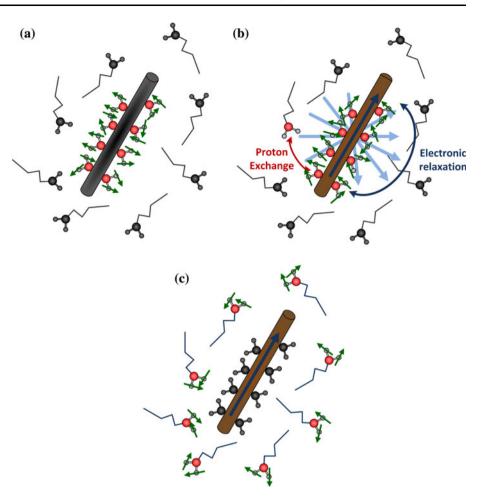
T_1 relaxation

Longitudinal relaxation of all the particles is caused by an inner sphere mechanism between the surface exchangeable protons and bulk water protons (see Fig. 8). This process is very similar to what happens for complexed paramagnetic ions, except that the correlations times of the modulation processes involved in the relaxation mechanism are somehow different. In our case the paramagnetic ions belong to a large particle whose rotation correlation time is very large compared to paramagnetic complexes. However, this situation is also happening for paramagnetic complexes linked to a large molecule, such as albumin. To understand the relaxation, the analysis of the NMRD profiles is useful. From the quantitative point of view, the relaxation induced by Dy-, Ho-, Er- and Tb-based particles is almost 100 times less efficient than for Gd-based particles. This is simply due to the different electron relaxation times of these ions in the particles: it is very short for the former group ($\ll 20$ ps), while it is quite long for the latter (176 ps), as shown by our EPR results. As the Solomon–Bloembergen inner-sphere relaxation rate is proportional, at low field, to the shortest correlation time, which is τ_e for Dy-, Ho-, Er- and Tb-based particles, the relaxation rate is rather small for these compounds, when compared to the gadolinium-containing particles. The constant high field relaxivity observed on the NMRD profiles, after the decrease of the relaxivity, is due to this Solomon–Bloembergen contribution (Fig. 8b). The amplitude of this constant high field relaxivity is compatible with previous observations for Ho^{3+}, Dy^{3+} and Er^{3+} ions even if the corresponding relaxivities are somehow smaller than in the study of Bertini et al. [57] at low fields (<1.5 T), probably because the core paramagnetic ions are not contributing to

the inner sphere relaxation process, which lowers the r_1 relaxivity of the particles. High-field measurements should show an increase of the longitudinal relaxivity as it is expected for these compounds, because of Curie relaxation [58]. The origin of the decrease of low field relaxivity is unclear. It corresponds to a long correlation time. The Solomon–Bloembergen inner-sphere theory does not predict this behavior because of fast electronic relaxation which should dominate all the other modulations of the dipolar interaction between the proton and the magnetic ion. The only relaxation mechanism independent of electron relaxation would be a simple dipolar coupling between protons on the particle's surface in a process similar to what is observed for solutions of diamagnetic proteins. In this case, the decrease of the relaxivity corresponds to proton exchange or particle rotation. Since almost the same correlation time is obtained for Dy-, Ho-, Er- and Tb-containing particles, we think—by elimination—that it is probably a proton exchange time (as illustrated in Fig. 8a). Indeed these different particles present very various sizes (from 150 to 1,500 nm) which should lead to very different rotation times. This interpretation for the low field relaxivity may seem tricky, but it is confirmed by the ^{2}H-NMRD profiles of the samples. Deuterium relaxation is due to the interaction of the ^{2}H electric quadrupolar moment with the electric field gradient at the nucleus. It is thus independent of the paramagnetic ion electronic relaxation. The correlation time associated with the observed ^{2}H-NMRD curve is almost the same for all the particles and it is similar to the correlation time obtained with ^{1}H-NMRD (except for Tb_4O_7 particles for an unknown reason). In our opinion, this confirms our interpretation of an exchange modulation for the ^{2}H quadrupole relaxation and for the adsorbed protons ^{1}H-^{1}H dipolar relaxation.

The electron relaxation of a gadolinium ion is known to be slower compared to Dy^{3+}, Ho^{3+}, Er^{3+} and Tb^{3+}. Our EPR results are providing τ_{2e} of 176 ps for Gd^{3+}. The usual inner sphere relaxation is thus dominant and the Curie relaxation is negligible. The shape of the NMRD profile (a simple lorentzian with a large offset) and the position of the dispersion for $Gd(OH)_3$ leads to a correlation time of 23.9 ns at 37 °C. However, as predicted by inner sphere theory, the first observed dispersion is an electronic dispersion with the inflection point at $\omega_S \tau = 1$, which leads to a correlation time of 36 ps. This value is far too short for the rotation time of the particle and the exchange time of protons. We will consider it as an electron relaxation time. The value obtained by ^{1}H-NMRD (36 ps) is however shorter than the EPR value (176 ps). Such a discrepancy could be explained by our crude fitting of the NMRD profile by a lorentzian function. Usually, the fitting procedure includes many parameters such as the distance of closest approach and the existence of a second

sphere of hydration [53]. Following our interpretation, a second dispersion is expected at higher field with a condition ($\omega_0 \tau = 1$), it should be observed at circa 3 GHz. This results in the large offset observed in the $Gd(OH)_3$ NMRD curve, reflecting the plateau of this high field dispersion.

T_2 relaxation

Gadolinium hydroxide particles are also distancing themselves from the other compounds in terms of the T_2 relaxation. Their transverse relaxation is due to a proton exchange between the particles' surface and bulk water protons. This relaxation process has already been noticed for anti-ferromagnetic ferritin and hydrated iron oxide particles resulting in a linear increase of $1/T_2$ with the magnetic moment of the particles and consequently with the external field B_0. This dependence is also observed for gadolinium hydroxide particles. However, the transverse relaxivities are not very large even at high fields. On the contrary, for all the other particles, the relaxation is caused by the diffusion of the water molecules in the gradients nearby the magnetic particles according to the outersphere relaxation mechanism (Fig. 8c). In this case $1/T_2$ is quadratically increasing with the magnetic fields which results in really interesting relaxivities at high magnetic fields. However, for very high fields the OSM is no more valid and the static dephasing regime model should be used instead, with a linear increase of the relaxation rate with the field. Our simulations show that the efficiency of the particles could be optimized by using spherical particles instead of rods. This could be achieved by using particles of different natures (rare-earth phosphate, fluoride...). Indeed, most of the oxide and hydroxide particles described in the literature are non spherical. The ideal T_2 contrast agent should be constituted of spherical holmium or dysprosium particles with a radius of about 40–50 nm. As in the outer-sphere regime the relaxivity is proportional to the square of the radius, very small paramagnetic particles ($R < 5$ nm) containing holmium, dysprosium, erbium or terbium won't be efficient at all, with $r_2 < 20$ s^{-1}mM^{-1} even at high fields, calculated from Eq. 4. At first sight, it is not clear why gadolinium-based particles are relaxing through an exchange in T_2 and the other samples through an outer sphere diffusion mechanism. It seems logical that if inner sphere and outer-sphere relaxation mechanisms are coexisting, inner sphere will dominate because of the smaller distance of approach. This is what happens for gadolinium-based particles. The real question is thus why is outer-sphere dominating inner sphere for the transverse relaxation of other particles? In our opinion this is caused by the difference in the electron relaxation times which cause negligible inner sphere relaxation rates for these

Fig. 8 Schemes of the different relaxation mechanisms occurring in the paramagnetic samples. Protons that don't contribute to the relaxation are in *grey color*. Cases **a** and **b** refer to longitudinal relaxation and case **c** to transverse relaxation. Case **a**: at sufficiently low field, the electronic magnetic moment of the paramagnetic particle is negligible and the relaxation is caused by the interaction between the magnetic moments of the hydrogen atoms (*green arrow*) that lie on the particle surface. The water molecules (in *grey*) diffusing around the particle don't contribute to the relaxation. Case **b**: at higher field, a proton exchange occurs at the surface of the particle and the proton magnetic moment (in *green*) interact with the electronic magnetic moment (in *blue*) that fluctuates because of the electronic relaxation. Case **c**: for the transverse relaxation, the relaxation mechanism is dominated by the bulk diffusion of proton around the magnetic moment of the paramagnetic particle

compounds compared to the outer-sphere contribution due to the mean magnetic moment of the whole particle.

Conclusions

The relaxation mechanisms of different kinds of paramagnetic particles have been investigated by experimental, simulation and theoretical approaches. Two different behaviors can be distinguished between the rare-earth oxides and hydroxides. On the one side, gadolinium-oxide (or hydroxide) nanoparticles whose longitudinal and transverse relaxation is caused by an inner-sphere mechanism, i.e. the exchange of protons between the particle surface and bulk water protons. On the other side, the dysprosium-, holmium-, erbium- and terbium-containing particles whose longitudinal relaxivity is very low (and explained by an inner-sphere mechanism), while their transverse relaxation is due to the diffusion of water molecules nearby the particles, in the so-called outer-sphere mechanism. These differences can be explained by the differences in the correlation times of the molecular tumbling involved in relaxation: exchange and electron relaxation. The understanding of the relaxation now allows giving advices for the development of the

paramagnetic particles for MRI: best T_1 agents will be realized with small particles of gadolinium oxide (or hydroxide). The shape and structure of the particles should be chosen in order to ensure the largest surface on volume ratio, as previously observed for gadolinium-fluoride particles [32]. Efficient T_2 agents could be obtained with dysprosium-, holmium-, terbium- and erbium-containing particles. Their size should be important, and their shape is preferably spherical as shown by the simulations results.

References

1. Modo MJM, Bulte JWM (2007) Molecular and cellular MR imaging. CRC Press, Cleveland
2. Aime S, Cabella C, Colombatto S, Crich SG, Gianolio E, Maggioni F (2002) Insights into the use of paramagnetic Gd(III)

complexes in MR-molecular imaging investigations. J Magn Reson Imaging 16:394–406

3. Jung CW, Jacobs P (1995) Physical and chemical properties of Superparamagnetic iron oxide MR contrast agents: ferumoxides, ferumoxtran, ferumoxsil. Magn Reson Imaging 13:661–674

4. Engstrom M, Klasson A, Pedersen H, Vahlberg C, Käll PO, Uvdal K (2006) High proton relaxivity for gadolinium oxide nanoparticles. Magn Reson Mater Phy Biol Med 19:180–186

5. Fortin MA, Petoral RM, Söderlind F, Klasson A, Engström M, Veres T, Käll PO, Uvdal K (2007) Polyethylene glycol-covered ultra-small Gd2O3 nanoparticles for positive contrast at 1.5 T magnetic resonance clinical scanning. Nanotechnology 18:395501

6. Arrais A, Botta M, Avedano S, Giovenzana GB, Gianolio E, Boccaleri E, Stanghellini PL, Aime S (2008) Carbon coated microshells containing nanosized Gd(III) oxidic phases for multiple bio-medical applications. Chem Commun (45):5936–5938

7. Norek M, Pereira GA, Geraldes CFGC, Denkova A, Zhou W, Peters JA (2007) NMR transversal relaxivity of suspensions of lanthanide oxide nanoparticles. J Phys Chem C 111:10240–10246

8. Norek M, Kampert E, Zeitler U, Peters JA (2008) Tuning of the size of DY2O3 nanoparticles for optimal performance as an MRI contrast agent. J Am Chem Soc 130:5335–5340

9. Gossuin Y, Hocq A, Vuong QL, Disch S, Hermann RP, Gillis P (2008) Physico-chemical and NMR relaxometric characterization of gadolinium hydroxide and dysprosium oxide nanoparticles. Nanotechnology 19:475102

10. Yin YD, Hong GY (2006) Synthesis and characterization of Gd(OH)(3) nanobundles. J Nanoparticle Res 8:755–760

11. Song XC, Zheng YF, Wang Y (2008) Selected-control synthesis of dysprosium hydroxide and oxide nanorods by adjusting hydrothermal temperature. Mater Res Bull 43:1106–1111

12. Zhang N, Yi R, Zhou L, Gao G, Shi R, Qiu G, Liu X (2009) Lanthanide hydroxide nanorods and their thermal decomposition to lanthanide oxide nanorods. Mater Chem Phys 114:160–167

13. Happy Tok AIY, Boey FYC, Huebner R, Ng SH (2006) Synthesis of dysprosium oxide by homogeneous precipitation. J Electroceramics 17:75–78

14. Happy Tok AIY, Su LT, Boey FYC, Ng SH (2007) Homogeneous precipitation of Dy2O3 nanoparticles-effects of synthesis parameters. J Nanosci Nanotechnol 7:907–915

15. Soliman SA, Abu-Zied BM (2009) Thermal genesis, characterization, and electrical conductivity measurements of terbium oxide catalyst obtained from terbium acetate. Thermochim Acta 491:84–91

16. Bazzi R, Flores-Gonzalez MA, Louis C, Lebbou K, Dujardin C, Brenier A, Zheng W, Tillement O, Bernstein E, Perriat P (2003) Synthesis and luminescent properties of sub-5-nm lanthanide oxides nanoparticles. J Lumin 102:445–450

17. Bridot JL, Faure A-C, Dayde D, Rivière C, Le Duc G, Billotey C, Janier M, Josserand V, Coll J-L, Perriat P, Roux S, Tillement O (2009) Hybrid gadolinium oxide nanoparticles combining imaging and therapy. J Mater Chem 19:2328–2335

18. Qian LW, Gui YC, Guo SA, Qiang G, Qian XF (2009) Controlled synthesis of light rare-earth hydroxide nanorods via a simple solution route. J Phys Chem Solids 70:688–693

19. Jia G, You H, Liu K, Zheng Y, Guo N, Jia J, Zhang H (2010) Highly uniform YBO3 hierarchical architectures: facile synthesis and tunable luminescence properties. Chem Eur J 16:2930–2937

20. Li L, Yang HK, Moon BK, Choi BC, Jeong JH, Kim KH (2010) Photoluminescent properties of Ln(2)O(3):Eu3+ (Ln = Y, Lu and Gd) prepared by hydrothermal process and sol-gel method. Mater Chem Phys 119:471–477

21. Petoral RM, Söderlind F, Klasson A, Suska A, Fortin MA, Abrikossova N, Selegård L, Käll P-O, Engström M, Uvdal K (2009) Synthesis and characterization of Tb3+-doped Gd2O3 nanocrystals: a bifunctional material with combined fluorescent

22. Dosev D, Nichkova M, Dumas RK, Gee SJ, Hammock BD, Liu K, Kennedy IM (2007) Magnetic/luminescent core/shell particles synthesized by spray pyrolysis and their application in immunoassays with internal standard. Nanotechnology 18:055102

23. Das GK, Heng BC, Ng S-C, White T, Loo JSC, D'Silva L, Padmanabhan P, Bhakoo KK, Selvan ST, Tan TTY (2010) Gadolinium oxide ultra narrow nanorods as multimodal contrast agents for optical and magnetic resonance imaging. Langmuir 26:8959–8965

24. Yoon YS, Lee B-I, Lee KS, Im GH, Byeon S-H, Lee JH, Lee IS (2009) Surface modification of exfoliated layered gadolinium hydroxide for the development of multimodal contrast agents for MRI and fluorescence imaging. Adv Funct Mater 19:3375–3380

25. Yoon YS, Lee B-I, Lee KS, Heo H, Lee JH, Byeon S-H, Lee IS (2010) Fabrication of a silica sphere with fluorescent and MR contrasting GdPO4 nanoparticles from layered gadolinium hydroxide. Chem Commun 46:3654–3656

26. Gossuin Y, Gillis P, Hocq A, Vuong QL, Roch A (2009) MR relaxation properties of superparamagnetic particles. Wiley Interdisciplinary Reviews—Nanomed Nanobiotechnol 1:299–310

27. Cullity BD, Graham CD (2008) Introduction to magnetic materials, 2nd edn. Wiley-IEEE Press, Hoboken

28. Klasson A, Ahrén M, Hellqvist E, Söderlind F, Rosén A, Käll P-O, Uvdal K, Engström M (2008) Positive MRI contrast enhancement in THP-1 cells with Gd2O3 nanoparticles. Contrast Media Mol Imaging 3:106–111

29. Bulte JWM, Kraitchman DL (2004) Iron oxide MR contrast agents for molecular and cellular imaging. NMR Biomed 17:484–499

30. Néel L (1948) Magnetic properties of ferrites: ferrimagnetism and antiferromagnetism. Ann Phys Paris 3:137–198

31. Ahrén M, Selegård L, Klasson A, Söderlind F, Abrikossova N, Skoglund C, Bengtsson T, Engström M, Käll P-O, Uvdal K (2010) Synthesis and characterization of PEGylated Gd2O3 nanoparticles for MRI contrast enhancement. Langmuir 26:5753–5762

32. Cheung ENM, Alvares RDA, Oakden W, Chaudhary R, Hill ML, Pichaandi J, Mo GCH, Yip C, Macdonald PM, Stanisz GJ, van Veggel FCJM, Cheung RSP (2010) Polymer-stabilized lanthanide fluoride nanoparticle aggregates as contrast agents for magnetic resonance imaging and computed tomography. Chem Mater 22:4728–4739

33. Choi ES, Park JY, Baek MJ, Xu W, Kattel K, Kim JH, Lee JJ, Chang J, Kim TJ, Bae JE, Chae KS, Suh KJ, Lee GH (2010) Water-soluble ultra-small manganese oxide surface doped gadolinium oxide (Gd2O3@MnO) nanoparticles for MRI contrast agent. Eur J Inorg Chem 28:4555–4560

34. Sánchez P, Valero E, Gálvez N, Domínguez-Vera JM, Marinone M, Poletti G, Corti M, Lascialfari A (2009) MRI relaxation properties of water-soluble apoferritin-encapsulated gadolinium oxide-hydroxide nanoparticles. Dalton Trans 5:800–804

35. Park JH, Baek MJ, Choi ES, Woo S, Kim JH, Kim TJ, Jung JC, Chae KS, Chang Y, Lee GH (2009) Paramagnetic ultrasmall gadolinium oxide nanoparticles as advanced T1 MRI contrast agent: account for large longitudinal relaxivity, optimal particle diameter, and in vivo T1 MR images. ACS Nano 3:3663–3669

36. Deo A, Fogel M, Cowper SE (2007) Nephrogenic systemic fibrosis: a population study examining the relationship of disease development to gadolinium exposure. Clin J Am Soc Nephrol 2:264–267

37. Stoll S, Schweiger A (2006) EasySpin, a comprehensive software package for spectral simulation and analysis in EPR. J Magn Reson 178:42–55

38. Gillis P, Moiny F, Brooks RA (2002) On T2-Shortening by strongly magnetized spheres: a partial refocusing model. Magn Reson Med 47:257–263

39. Vuong QL, Gillis P, Gossuin Y (2011) Monte Carlo simulation and theory of proton NMR transverse relaxation induced by aggregation of magnetic particles used as MRI contrast agents. J Magn Reson 212:139–148

40. Yin S, Akita S, Shinozaki M, Li R, Sato T (2008) Synthesis and morphological control of rare earth oxide nanoparticles by solvothermal reaction. J Mater Sci 43:2234–2239

41. Zhang J, Liu ZG, Lin J, Fang JY (2005) Y2O3 microprisms with trilobal cross section. Cryst Growth Des 5:1527–1530

42. McIntyre LJ, Prior TJ, Fogg AM (2010) Observation and isolation of layered and framework ytterbium hydroxide phases using in situ energy-dispersive X-ray diffraction. Chem Mater 22:2635–2645

43. Fang Y-P, Xu A-W, You L-P, Song R-Q, Yu JC, Zhang H-X, Li Q, Liu H-Q (2003) Hydrothermal synthesis of rare earth (Tb, Y) hydroxide and oxide nanotubes. Adv Funct Mater 13:955–960

44. (1977) Handbook of chemistry and physics. CRC Press, Cleveland

45. Gossuin Y, Roch A, Muller RN, Gillis P (2002) An evaluation of the contributions of diffusion and exchange in relaxation enhancement by MRI contrast agents. J Magn Reson 158:36–42

46. Mc Connel J (1987) The theory of nuclear magnetic relaxation in liquids. Cambridge university press, Cambridge

47. Satoh A, Chantrell RW, Kamiyama S-I, Coverdale GN (1996) Two-dimensional Monte Carlo simulations to capture thick cha-inlike clusters of ferromagnetic particles in colloidal dispersions. J Colloid Interface Sci 178:620–627

48. Platas-Iglesias C, Vander Elst L, Zhou W, Muller RN, Geraldes CFG, Mashmeyer T, Peters JA (2002) Zeolite GdNaY nanoparticles with very high relaxitivity for application as contrast agents in magnetic resonance imaging. Chem Eur J 8:5121–5131

49. Brodbeck CM, Iton LE (1985) The EPR spectra of Gd3+ and Eu2+ in glassy systems. J Chem Phys 83:4285

50. Du G, Van Tendeloo G (2005) Preparation and structure analysis of Gd(OH)3 nanorods. Nanotechnology 16:595–597

51. Reuben J (1975) Electron spin relaxation in aqueous solutions of gadolinium(III)-aquo, cacodylate and bovine serum albumin complexes. J Phys Chem 75:3164

52. Toth E, Helm L, Kellar KE, Merbach AE (1999) Gd(DTPA-bisa-mide)alkyl copolymers: a hint for the formation of MRI contrast agents with very high relaxivity. Chem Eur J 5:1202–1211

53. Zitha-Bovens E, Muller RN, Laurent S, Vander Elst L, Geraldes CFGC, van Bekkum H, Peters JA (2005) Structure and dynamics of lanthanide complexes of TTHA and TTHA-bisamides as studied by NMR, NMRD and EPR. Helv Chim Acta 88:618–632

54. Brovelli S, Chiodini N, Meinardi F, Lauria A, Lorenzi R, Vo-dopivec B, Mozzati MC, Paleari A (2009) Confined diffusion of erbium excitations in SnO2 nanoparticles embedded in silica: a time-resolved infrared luminescence study. Phys Rev B 79: 153108

55. Dantelle G, Mortier M, Vivien D (2007) EPR and optical studies of erbium-doped βPbF2 single crystals and nanocrystals in transparent oxyfluoride glass-ceramics. Phys Chem Chem Phys 9:5591–5598

56. Abragam A, Bleaney B (1970) Electron paramagnetic resonance. Clarendon press, Oxford

57. Bertini I, Capozzi F, Luchinat C, Nicastro G, Xia Z (1993) Water proton relaxation for some lanthanide aqua ions in solution. J Phys Chem 97:6351–6354

58. Gueron M (1975) Nuclear relaxation in macromolecules by paramagnetic ions: a novel mechanism. J Mag Reson 19:58–66